



HAL
open science

A Hybrid Numerical Approach for Characterising Airflow and Temperature Distribution in a Ventilated Pallet of Heat-Generating Products: Application to Cheese

Dihia Aguenihanai, Denis Flick, Steven Duret, J. Moureh

► **To cite this version:**

Dihia Aguenihanai, Denis Flick, Steven Duret, J. Moureh. A Hybrid Numerical Approach for Characterising Airflow and Temperature Distribution in a Ventilated Pallet of Heat-Generating Products: Application to Cheese. *Journal of Food Engineering*, 2025, 387, pp.112323. 10.1016/j.jfoodeng.2024.112323 . hal-04703396

HAL Id: hal-04703396

<https://hal.inrae.fr/hal-04703396v1>

Submitted on 20 Sep 2024

HAL is a multi-disciplinary open access archive for the deposit and dissemination of scientific research documents, whether they are published or not. The documents may come from teaching and research institutions in France or abroad, or from public or private research centers.

L'archive ouverte pluridisciplinaire **HAL**, est destinée au dépôt et à la diffusion de documents scientifiques de niveau recherche, publiés ou non, émanant des établissements d'enseignement et de recherche français ou étrangers, des laboratoires publics ou privés.



Distributed under a Creative Commons Attribution 4.0 International License

A Hybrid Numerical Approach for Characterising Airflow and Temperature Distribution in a Ventilated Pallet of Heat-Generating Products: Application to Cheese

Dihia AGUENIHANAI^{*(a,b)}, Denis FLICK^(c), Steven DURET^(a), Jean MOUREH^(a)

^(a) Université Paris-Saclay, INRAE, FRISE, 92761 Antony, France

^(b) CNIEL, 75009 Paris, France

^(c) Université Paris-Saclay, INRAE, AgroParisTech, UMR SayFood, 91120 Palaiseau, France

*Corresponding author: dihia.aguenihanai@inrae.fr

Abstract

Temperature control throughout the cold chain is of crucial importance in the preservation of the quality of cheese. As a result of cheese heat generation, both natural and forced convection need to be considered. This numerical study aimed to characterise the airflow and temperature fields within a ventilated pallet of heat-generating cheeses. An original computational fluid dynamics (CFD) hybrid approach was developed. This approach is based on a combination of a porous media approach for the contents of the boxes and a direct CFD approach for the outer cardboard walls, including vent size and position. The computational domain is limited to one pallet level. The simulations were conducted on a steady state for two upwind air velocities 0.31 m/s and 0.73 m/s and three generated heat fluxes 0.05 W, 0.15 W, and 0.3 W per product item (250 g). The model was validated by comparison with experimental results related to velocity and product temperature profiles obtained on a full-scale experimental set-up. The hybrid approach shows good accuracy while reducing the mesh size and the computational time in comparison with the direct CFD approach.

Keywords: Heat-generating products, mixed convection, porous medium, direct CFD, hybrid approach

Nomenclature

C_p	Heat capacity at constant pressure, $J\ kg^{-1}\ K^{-1}$
D	Cheese diameter, m
F	Forchheimer coefficient, [-]
K	Permeability, m^2
k	Turbulent kinetic energy, m^2/s^2
$\varnothing_{z,in}$	Vertical airflow rate, m^3/s
p	Pressure, Pa
Q	Heat generation flux per product item (250 g of camembert), W
$Q_{heat,tot}$	Heat generation for one carton (30 camemberts), W

$Q_{\text{heat.tot}}$	Volumetric heat generation for one carton, W/m^3
S	Momentum source term, $\text{kg}/(\text{m s})^2$
$S_{\text{interface}}$	Interface surface between the porous zone and the air gap, m^2
T	Temperature, $^{\circ}\text{C}$
u	Air velocity, m/s
u_z	Vertical component of the airflow velocity, m/s
V	Volume, m^3
β_T	Thermal expansion coefficient, K^{-1}
ν	Kinematic viscosity, m^2/s

Abbreviations

CFD	Computational Fluid Dynamics
FV	Front vent
LDV	Laser Doppler Velocimetry
REV	Representative Elementary Volume
RMSE	Root Mean Square Error, $^{\circ}\text{C}$

Dimensionless numbers

Gr	Grashof number, [-]
Pr	Prandtl number, [-]
Ra	Rayleigh number, [-]
Re	Reynolds number, [-]
Ri	Richardson number, [-]

Greek symbols

ε	Turbulence dissipation rate, m^2/s^3
ε_f	Fluid porosity of stacked cheese: $\varepsilon_f = V_f/V_{\text{tot}}$, [-]
λ	Thermal conductivity, $\text{W}/(\text{m K})$
μ	Dynamic viscosity, $\text{kg m}^{-1}/\text{s}$
ρ	Density, kg/m^3
ω	Specific turbulent dissipation rate, s^{-1}

Subscripts

air.in	Upwind airflow
d	driving
exp	Experimental
f	Fluid
max	Maximum
num	Numerical
out	Outlet

p	Porous media
t	Turbulent
tot	Total

25 1. Introduction

26 The temperature of cheese within pallets must be controlled and maintained below a
 27 recommended value throughout the cold chain to preserve quality and reduce losses (Pham et al., 2019).
 28 In the forced convection regime at the beginning of the cold chain (precooling), temperature
 29 heterogeneity can be encountered within stacks such as pallets, depending on several parameters such
 30 as the airflow rate (Wang et al., 2020), stacking pattern (Moureh et al., 2009b), ventilated box
 31 configuration including vent hole design and the total area of the openings (Berry et al., 2021). Heat
 32 generation induced by the respiration activity of the products can enhance natural convection and affect
 33 the level and heterogeneity of the product temperature. It is important to take this aspect into account,
 34 particularly in the case of periods during which the air velocity is low, such as during storage, where
 35 forced convection can be dominated by natural convection (Pham et al., 2021), of polylined products
 36 (O’Sullivan et al., 2017), and during long precooling processes (Redding et al., 2016).

37 Soft cheese products such as “*Camemberts*” contain lactic ferments and continue their
 38 metabolism once the products have been conditioned. As a result of the metabolic activity (respiration)
 39 of the micro-organisms, they generate heat (Hélias et al., 2008; Pham, 2021). This heat generation due
 40 to product respiration depends on the product temperature (Delele et al., 2013; Han et al., 2015) and can
 41 vary from one product to another. Recently, Pham et al. (2021) studied the effect of the natural
 42 convection induced by the respiration heat of cheese on the temperature of products within one level of
 43 a pallet. The study showed that products under mixed convection regime are better cooled than those
 44 under a forced regime. Chourasia and Goswami (2007) obtained similar results and showed that
 45 recirculation due to natural convection helps remove heat from the products, leading to a lower product
 46 temperature. Thus, natural convection exerts a positive influence on the heat transfer within a product
 47 stack.

48 Several experimental studies have been conducted to better understand and evaluate the cooling
 49 behaviour of stacks of products (Duret et al., 2014; Praeger et al., 2020). These studies represent real
 50 conditions and consider the random arrangement of products within a cardboard box and the spaces
 51 between ventilated boxes which can affect the connection between successive holes under real
 52 ventilation conditions. Nevertheless, there are few such studies in the literature because of their cost and
 53 the required manual handling time (Zou et al., 2006a). Computational Fluid Dynamics (CFD) modelling
 54 is therefore used to avoid the complexity of implementing experiments or to reduce the number of
 55 experiments.

56 Two main CFD methods are the most widely used: the direct CFD and porous media approaches.
 57 Both numerical approaches have their advantages and drawbacks. The direct CFD approach explicitly

58 reproduces both ventilated box geometry and product shapes and their arrangements. As it explicitly
59 solves the local heat transfer and fluid transport, it accurately predicts the characteristics of local airflow
60 through vent holes and around products as well as the product temperature level and heterogeneity
61 within the stack. However, it involves a large number of meshes and a high computational cost. Hence,
62 it is limited to a small computational domain, such as one box (Wang et al., 2020), one pallet level (Han
63 et al., 2018), and rarely one pallet (Wu et al., 2019).

64 To manage computational resource issues, a porous medium approach has been used to model
65 large domains such as cold rooms (Hoang et al., 2015) and transport vehicles (Moureh et al., 2009a).
66 This method simplifies the geometry and models the flow roughly with a reduced computational time
67 and an acceptable accuracy. According to Hoang et al. (2015), results obtained from modelling four
68 pallets within a cold room using porous media, the relative error between numerical and experimental
69 values of Nusselt number and velocity are 15% and 44%, respectively. However, this approach lacks
70 sensitivity in modelling local airflow behaviour, issuing vent holes and temperature characteristics
71 within boxes or stacks (Zou et al., 2006b). It involves integrating the conservation equations in the
72 porous region. The airflow in the porous medium is characterized by its superficial velocity determined
73 through local volume averaging. In addition, it requires the determination of additional parameters
74 related to the pressure drop coefficients (often by using the Darcy-Forchheimer equation) and the heat
75 transfer coefficient in the case of Local Thermal Non-Equilibrium (LTNE) modelling (Zhao et al., 2016;
76 Alvarez et al., 2003; Hoang et al., 2015). Furthermore, (Pham et al., 2021) and (Ambaw et al., 2017),
77 showed that pressure losses are located at the vents of boxes for a stack of products. This highlights the
78 importance of modelling the packaging details (vents position, size and shape) to better characterise
79 local airflow behaviour, which in turn has an impact on temperature distribution within the stack.

80 To overcome the limitations of both the direct CFD (mainly related to calculation resources
81 limitations for a large-scale modelling) and porous medium approaches (lack of sensitivity in modelling
82 local airflow behaviour), this study aimed to develop an original hybrid approach applied to a single
83 pallet level of heat-generating cheese. This new method combines the porous media method for the
84 contents of the boxes (cheeses) and the direct CFD approach to explicitly model the ventilated cartons,
85 including vent design, size, and positions. A previous numerical study was carried out by Pham et al.
86 (2021) on the same computational domain (one level pallet of cheese generating heat) using direct CFD
87 approach. It involved a computational time of 48 hours and a mesh size of 10^7 cells. Both studies take
88 into account forced convection and natural convection promoted by cheese heat generation.

89 The objectives of this study were to evaluate the ability of the hybrid approach in reducing
90 calculation time while ensuring accuracy of the airflow and temperature prediction. The hybrid approach
91 will help to gain a better insight into local airflow behaviour, notably for the interaction of small jets
92 through vent holes with the porous stack of product, while reducing mesh size and computing time. The
93 results obtained using this new approach were evaluated and compared to the experimental and

94 numerical results obtained by Pham et al. (2021). Different conditions of air velocity and heat generation
95 were tested to evaluate the approach performances, discuss its limitations and identify future research.

96 **2. Materials and methods**

97 **2.1 Experimental device and measurements**

98 The experimental device consists of one cheese pallet with industrial dimensions (800 mm ×
99 1200 mm × 1455 mm) placed within a cold room with 5100 mm × 3200 mm × 2860 mm dimensions
100 subjected to ambience parameter (temperature and velocity) control. The temperature of the cold room
101 was set at $T_{\text{air.in}} = 4^{\circ}\text{C}$. The pallet was composed of nine levels with six cardboard boxes of product per
102 level. A space of about 10 mm separated the boxes placed at the same level. Each cardboard box
103 contained 30 cheeses superposed in three layers and arranged in two rows (see Fig. 2). Each product (D
104 = 110 mm, $H = 40$ mm) weighed 250 g and generated heat flux Q . In order to ensure both experimental
105 stability conditions and repeatability, cylindrical plaster products equipped with controllable heating
106 resistances were used to represent cheese products (camembert) and their heat generation; more details
107 can be found in (Pham et al., 2019).

108 The experimental measurements used in this study were obtained by Pham et al. (2021). The
109 transversal air velocity was measured at the mid-height of the air gap using Laser Doppler Velocimetry
110 (LDV). The temperature of the products was measured on the axis of the cheese at 45 mm from the top
111 using T-Type thermocouples with an accuracy of ± 0.1 K (precision: ± 0.05 K) after individual
112 calibration between 273 and 293 K (Pham et al., 2021) (see Fig. 1).

113 **2.2 Numerical modelling**

114 **2.2.1 Computational domain**

115 In this study, a three-dimensional (3D) CFD model was developed and applied at steady state.
116 Based on the same computational domain as Pham et al. (2021), the interactions between the different
117 levels of the pallet were not taken into account. The model is limited to one level (see Fig. 2). Therefore,
118 the bottom vents of the cardboard box were not considered.

119 The space between the cardboard boxes was included in the 3D geometry. A previous steady-
120 state study by Pham et al. (2021) was performed on the same computational domain (one pallet level)
121 using a direct CFD approach. This study considered a cardboard box with the same shape and size,
122 including its vents, as that used by Pham et al. (2021).

123 **2.2.2 Hybrid approach versus direct CFD approach**

124 The simulations applied in this study were conducted using a new method called the hybrid
125 approach. This method aims to combine in the same model the two most commonly used modelling
126 methods: direct CFD and porous media approaches. As shown in Fig. 3, this original approach involves
127 modelling the internal part of the cheese package (i.e., cheese and surrounding air) as a porous zone,

128 while the cardboard box, including its vent sizes and positions, is explicitly modelled using the direct
129 CFD approach. The modelling of the box vent details (design and positions) allows better predictions
130 for local jet trajectories and preferential air paths. According to Pham et al. (2021) and Ambaw et al.
131 (2017), pressure drop due to product stacking is negligible, whereas the pressure drop across vents is
132 more significant. Also, the validation of this approach allows the modelling of an entire pallet or a load
133 of pallets, including their mutual interactions (which is hardly possible with the direct CFD method).

134 In addition, it is important to underline that to accurately capture the behaviour of a system, the
135 representative elementary volume (REV) must be significantly larger than the pore scale or the fruit
136 diameter (Defraeye et al., 2022) but still much smaller than the overall dimensions of the macroscopic
137 flow domain (Nield and Bejan, 2017). According to Zhao et al. (2016), the continuous-medium
138 assumption becomes questionable, especially when the ratio of package-to-produce diameter is less than
139 10 which often occurs in the case of individual packages of cheese. In these cases, the heterogeneity of
140 the local airflow pattern within packages exerts a major impact on the transport phenomena (Ferrua and
141 Singh, 2008). More the product diameter is high, more the deviation with real configuration become
142 potentially high.

143 The calculated fluid porosity of one box of products is 34.5% (porosity calculation details were
144 added to the supplementary material section). In order to simplify the geometry and reduce
145 computational time, the thickness of the walls of the cardboard box was not considered in the modelling
146 domain. Nevertheless, its thermal resistance effect on the convective heat transfer between the product
147 and the ambience was taken into account.

148 The direct CFD method used by Pham et al. (2021) is based on detailed modelling of box and
149 product geometry of one pallet level. It, therefore, provides results with a good accuracy in comparison
150 with experimental results but requires considerable computing time (48 hours for the modelling of a
151 single pallet level).

152 Product heat generation (Q per cheese item) and induced natural convection are taken into
153 account in both direct CFD and hybrid approaches. For the direct CFD method, the heat generation is
154 considered uniform in each camembert. For the hybrid method, heat generation is considered as uniform
155 within the porous zone domain.

156 To validate the model and compare the two approaches, hybrid and direct CFD, the results
157 obtained using this new approach related to the airflow velocity and product temperature were compared
158 to the experimental and numerical results obtained by Pham et al. (2021). Fig. 1 summarises the
159 positions at which temperature and velocity measurements were performed for this comparison:

- 160 • The transversal air velocity profiles along the lines $L_{i \in \{1, 3\}}$ for the three cartons (or boxes).
- 161 • The temperature of the products along the line L_T .

162 **2.2.3 Modelling conditions and thermophysical properties of the materials**

163 The modelling conditions of this numerical study were identical to those used by Pham et al.
 164 (2021). The simulations were performed for two air upwind velocities $u_{air.in}$: 0.31 m/s and 0.73 m/s and
 165 three heat generation per product item Q : 0.05 W, 0.15 W and 0.3 W. According to an internal
 166 calorimetry study of the heat generation of 250 g of camembert products, the measured heat generation
 167 of this type of cheese is estimated between 0.1W and 0.15W (unpublished report (Delahaye et al., 2019)).
 168 This result is in agreement with the calculations using the data of Hélias et al. (2007) and Gaucel et al.
 169 (2012), where the calculated heat-generated flux of 250 g of cheese is estimated to be 0.1 W.

170 Depending on the pallet position and the cold chain facilities, such as transport and storage
 171 stages, the airflow velocity can vary from 0.1 m/s (or even less) to 1 m/s (Hoang et al., 2015; Moureh et
 172 al., 2009b). Thus, the Richardson number during the storage can vary between 0.14 and 13.61 ($Q = 0.1$
 173 W and $0.1 \text{ m/s} \leq u_{air.in} \leq 1 \text{ m/s}$). However, the upwind air velocities in the experimental cold room cannot
 174 be lower than 0.31 m/s. In order to: 1) obtain a Richardson number closer to the range of industrial
 175 values and 2) take into consideration the thermal runaway conditions of cheese products during the cold
 176 chain (Leclercq-Perlat et al., 2012), the choice was made to adjust the heat flux. Three heat fluxes were
 177 chosen: 0.05W, 0.15W and 0.3W ($0.13 \leq Ri \leq 4.25$).

178 Table 1 summarises the dimensionless numbers Re , Re_p and Ri for the different conditions.

179 *Table 1: Dimensionless numbers of the model.*

$u_{air.in}$ (m/s)	Re (-)	Re_p (-)	Q (W)	Ri (-)
0.31	2172	6296	0.05	0.71
			0.15	2.12
			0.3	4.25
0.73	5115	14825	0.05	0.13
			0.15	0.38
			0.3	0.77

180
181

$$Re_p = \frac{u_{air.in} D}{\nu \epsilon_f} \quad (1)$$

182

$$Re = \frac{u_{air.in} D}{\nu} \quad (2)$$

183

$$Gr = \frac{g\beta_T Q D^2}{\lambda \nu^2} \quad (3)$$

184

$$Ri = \frac{Gr}{Re^2} = \frac{g\beta_T Q}{\lambda u_{air.in}^2} \quad (4)$$

185 where: $v = 15.7 \times 10^{-6} \text{ m}^2/\text{s}$; $\varepsilon_f = 0.345$; $\lambda = 0.026 \text{ W}/(\text{m K})$; $\beta_T = 1/T_{air.in} = 0.00336 \text{ K}^{-1}$; the diameter D
 186 is considered equal to the diameter of the camemberts: $D = 0.11 \text{ m}$.

187 As shown in Table 1, the Reynolds number related to porous medium (Re_p) is higher than 300.
 188 Therefore, the airflow regime in the camembert stack for both air upwind velocities is turbulent (Delele
 189 et al., 2013; Einfeld and Schnitzlein, 2001; Nield and Bejan, 2017). Furthermore, according to Bejan
 190 (2013), the critical Reynolds number for round jet flows is about 30. In this study, the Reynolds number
 191 through round vents of the box with a minimum diameter of 15 mm (Pham et al., 2019) is $Re_{vents} = 296$
 192 ($D_{min.vents} = 15 \text{ mm}$; $u_{air.in} = 0.31 \text{ m/s}$).

193 Mixed convection is considered when $Ri \approx 1$. The airflow is dominated by forced convection at
 194 a low Richardson number $Ri < 0.1$ and by natural convection at a high Richardson number $Ri > 10$.

195 The thermal conductivity of the plaster and of the corrugated cardboard are $0.35 \text{ W}/(\text{m K})$ (data
 196 from the manufacturer) and $0.064 \text{ W}/(\text{m K})$ (data from Ho et al. (2010)), respectively. In addition, it's
 197 important to mention that the thermal conductivities of plaster and cheese are close: between 0.32 and
 198 $0.38 \text{ W}\cdot\text{m}^{-1}\text{K}^{-1}$ for cheese depending on the type of cheese (Iezzi et al., 2011). This leads to similar
 199 temperature levels at steady state between cheese and plaster.

200 2.2.4 Assumptions

201 Some simplifications and assumptions were made to reduce the computational cost while
 202 providing a good system representation.

- 203 • The airflow was considered incompressible and turbulent ($Re_p > 300$) (Delele et al., 2013; Nield
 204 and Bejan, 2017).
- 205 • Natural convection was taken into account using the Boussinesq approximation.
- 206 • The respiration heat flux per product item (Q) is considered independent of the temperature. It
 207 is used to identify the volumetric source term $q_{heat.tot} = Q_{heat.tot}/V_P$, where $Q_{heat.tot} = 30 Q$.
- 208 • The heat source term related to cheese respiration is assumed uniform on the porous zone.
- 209 • With the exception of the density variation in the buoyancy term assumed by the Boussinesq
 210 approximation, the thermophysical properties of both phases of the porous media are assumed
 211 to be constant and independent of the temperature.
- 212 • As the flow rate was high ($Re \gg 1$), the airflow resistance characteristics of the porous zone
 213 were established using Darcy- Forchheimer law (Verboven et al., 2006).
- 214 • Local Thermal Equilibrium (LTE) between the two phases of the porous media is assumed. It
 215 should be borne in mind that LTE is not strictly verified in the case of products generating heat
 216 (Verboven et al., 2006). Nevertheless, Delele et al. (2013) applied this assumption to grapes
 217 with respiration activity estimated to $49 \text{ W}/\text{m}^3$ and $4.35 \text{ W}/\text{m}^3$ for a product temperature of 21°C

218 and -0.5°C , respectively. Numerical results for the product temperature showed good accuracy
 219 compared to experimental data, with a relative error of 17.5%.

220 2.2.5 Governing equations

221 The direct CFD approach solves locally the conservation equation of momentum (Reynolds
 222 time-Averaged Navier-Stokes) and energy for the air outside and inside the boxes. The interaction
 223 between air and product is ensured by the boundary conditions at the surface of the product items. With
 224 the porous media approach, air outside the boxes is treated in the same way, but inside the boxes the
 225 local volume-averaged conservation equation of momentum is solved. The interaction between air and
 226 product is taken into account by the Darcy-Forchheimer terms whose coefficients have to be determined
 227 specifically. The hybrid model includes heat generation of products and the promoted natural convection
 228 and assumes the local thermal equilibrium for the heat transfer resolution. The steady-state heat transfer
 229 and incompressible flow were solved using Reynolds Averaged Navier-Stokes (RANS) equations
 230 combined with a turbulence model.

- 231 • RANS Mass conservation equation

$$\frac{\partial \bar{u}_i}{\partial x_i} = 0 \quad (5)$$

- 232 • RANS momentum conservation equation

233 After the application of the Boussinesq approximation, the conservation equation of the
 234 momentum is given by:

$$\rho_0 \frac{\partial(\bar{u}_i \bar{u}_j)}{\partial x_j} = -\frac{\partial \bar{p}_d}{\partial x_i} + \frac{\partial}{\partial x_j} \left[\mu_f \left(\frac{\partial \bar{u}_i}{\partial x_j} + \frac{\partial \bar{u}_j}{\partial x_i} \right) \right] - \frac{\partial}{\partial x_j} (\rho_0 \overline{u_i' u_j'}) - \rho_0 \beta_T (T_f - T_0) g_i + \bar{S}_{p,i} \quad (6)$$

235 where:

236 (T_0, ρ_0) are the fluid temperature and the density at the reference state (air inlet).

237 $\bar{S}_{p,i}$ is a momentum source term that characterises the flow resistance in the porous medium. For
 238 a homogenous porous media, it is defined by the following Darcy-Forchheimer law:

$$\bar{S}_{p,i} = -\frac{\mu_f}{K} \bar{u}_i - \rho_0 \frac{F}{\sqrt{K}} |\bar{u}| \bar{u}_i \quad (7)$$

239 Viscous and inertial pressure drop coefficients are also used instead of K and F:

240 $C_1=1/K$: Viscous pressure drop coefficient [$1/\text{m}^2$]

241 $C_2=F/K^{1/2}$: Inertial pressure drop coefficient [$1/\text{m}$]

242

243 The Reynolds tensor $\overline{u_i' u_j'}$ can be approximated as below:

$$\overline{u_i' u_j'} = -\frac{\mu_t}{\rho_0} \left(\frac{\partial \bar{u}_i}{\partial x_j} + \frac{\partial \bar{u}_j}{\partial x_i} \right) + \frac{2}{3} k \delta_{ij} \quad (8)$$

244 • RANS energy conservation equation

$$\rho_0 C_{p_f} \bar{u}_1 \frac{\partial \bar{T}}{\partial x_i} = \frac{\partial}{\partial x_i} \left[\lambda_{\text{eff}} \left(\frac{\partial \bar{T}}{\partial x_j} \right) \right] - \rho_0 C_{p_f} \frac{\partial}{\partial x_i} (\overline{u_1' T'}) + q_{\text{heat-tot}} \quad (9)$$

$$\lambda_{\text{eff}} = (1 - \varepsilon_f) \lambda_s + \varepsilon_f \lambda_f$$

246 The turbulent heat flux ($\overline{u_1' T'}$), can be expressed as follows:

$$\overline{u_1' T'} = - \frac{\mu_t}{\rho_0 \text{Pr}_t} \left(\frac{\partial \bar{T}}{\partial x_j} \right) \quad (10)$$

247 According to the k- ε turbulence model, the turbulent viscosity μ_t is related to turbulence kinetic
248 energy (k) and its dissipation rate (ε).

$$\mu_t = \rho_0 C_\mu \frac{k^2}{\varepsilon} \quad (11)$$

249 The k- ω turbulence model is given as:

$$\mu_t = \rho_0 C_\mu \frac{k}{\omega} \quad (12)$$

250 2.2.6 Boundary conditions

251 As the numerical results of this present study were to be compared to the numerical and
252 experimental results of Pham et al. (2021), the same boundary conditions were assumed related to an
253 upwind air velocity $u_{\text{air.in}}$ and a temperature of 4°C, at the inlet and an atmospheric pressure, at the outlet.
254 The wall boundaries of the channel were assumed as adiabatic no-slip walls (see Fig. 2). Concerning the
255 boxes walls, they were considered as non-slip walls with coupled heat transfer with the surrounding
256 environment (cheese/porous zone on one side and ventilated airflow on the other side).

257 2.2.7 Simulation parameters

258 Anisotropic Darcy Forchheimer coefficients (Table 2) were determined numerically using a
259 direct CFD approach. More details on the determination of these coefficients have been added in the
260 supplementary material section.

261 *Table 2: Isotropic Darcy-Forchheimer coefficient.*

Directions	C_1 [1/m ²]	C_2 [1/m]
x	1.65×10^7	5.35×10^2
y	5.01×10^6	1.68×10^2
z	1.75×10^5	5.26×10^1

262 2.2.8 Simulation set-up

263 The simulations were performed using Ansys Fluent 2021 CFD software on a 64-bit Windows
264 10 computer with processor Intel® Xeon® W- 2133 CPU @ 3.60GHz and 256 GB installed RAM with

265 12 cores. The simulations were performed at steady state. The chosen solving algorithm is “Coupled”;
266 the upwind 2nd order scheme was used for the momentum and energy discretisation, and the upwind 1st
267 order was adopted for the turbulent dissipation and kinetic energy.

268 In this study, different mesh sizes were tested: 9.63×10^3 , 4.90×10^4 , 8.29×10^5 , 1.60×10^6 ,
269 1.92×10^6 , 2.49×10^6 and 7.35×10^6 cells. The mesh sensitivity simulations were performed for
270 $u_{\text{air.in}}=0.73$ m/s and $Q = 0.3$ W. As a compromise between computational time and the accuracy of the
271 results, the mesh size adopted in this study was 8.29×10^5 . The calculation time for the chosen mesh
272 was about 4 hours, whereas when the direct CFD approach was used, the calculation time was about 48
273 hours for the same calculation domain (10^7 cells) (Pham et al., 2021).

274 In addition, four turbulence models were tested (standard k- ϵ , RNG k- ϵ , realizable k- ϵ and SST
275 k- ω) for two configurations (0.31 m/s & 0.3W and 0.73 m/s & 0.3W). Standard k- ϵ model was chosen
276 as it offers a better compromise for both cases.

277 More details about mesh and turbulence model sensitivity have been added in supplementary
278 material section.

279 The numerical results of this study were compared to the experimental data of Pham et al. (2021)
280 using RMSE (Root Mean Square Error) calculated as follows:

$$\text{RMSE} = \sqrt{\frac{1}{N} \sum_{n=1}^N (T_{p.\text{num},n} - T_{p.\text{exp},n})^2} \quad \text{for } N = 6 \quad (13)$$

281 $T_{p.\text{num},n}$ is the temperature taken at a depth of 45 mm within the porous medium at the same
282 position considered in experiments (at different positions of camemberts $n \in [1, 6]$) (see Fig. 1).

283 3. Results and discussion

284 3.1.1 Airflow distribution

285 Fig. 4 compares the dimensionless transversal velocities obtained using the hybrid approach
286 ($u_x^* = u_x / u_{\text{air.in}}$) with the experimental measurements and direct CFD results obtained by Pham et al.
287 (Pham et al., 2021). The transversal velocity is obtained along the lines L_1 , L_2 and L_3 located at the mid-
288 height of the air gap of the boxes B_1 , B_2 and B_3 , respectively (see Fig. 1), for the air upwind velocity,
289 0.31 m/s and both heat fluxes 0.05 W and 0.3 W.

290 According to Fig. 4, the hybrid approach, similarly to the direct CFD approach results, shows
291 reasonable agreement with the experimental results. In addition, the differences between the two models
292 could be explained by the fact that the porous medium induces a global homogenisation of the cheese
293 domain, implying less peak velocities in the air headspace than the direct CFD approach due to the local
294 jet diffusion in the porous medium.

295 The peaks of the velocity profiles in Fig. 4 reflect the presence of the front vents FV_1 , FV_2 and
296 FV_3 located in the headspace at the top of the box, which behave as air jets supplying the air layer above

297 the cheese with relatively high local velocities. For both heat fluxes, the velocity peaks in the air layer
298 of the upstream ventilated box B_1 are of almost the same order as the inlet velocity. In the principal vent
299 FV_2 , $u_x^* \approx 0.9$ for 0.05 W and $u_x^* \approx 0.8$ for 0.3 W. Based on the analysis of the inflow and outflow rates
300 through the front and side vents (Fig. 5b), the airflow enters through the front and side vents across the
301 symmetry plane resulting from the 10 mm space between the boxes. When comparing velocity profiles
302 along L_1 , L_2 and L_3 (Fig. 4) and according to the distribution of velocity magnitude at mid-height of the
303 headspace as shown in Fig. 5a, the air velocity decreases from upstream to downstream through the
304 boxes. This decrease can be explained by the deflection of the main flow towards the lateral side and its
305 exit through the spaces between boxes B_1 , B_2 and B_3 , as the total outflow from B_1 is higher than the total
306 inflow into B_2 , as well as from B_2 into B_3 (Fig. 5b). This gives rise to strong pathways between the front
307 and side vents where an important part of the main upstream flow exits the pallet domain through side
308 vents, which in turn reduces the peak velocities of the main flow. The strongest short circuit is observed
309 for FV_1 due to its close proximity to the side vent located in the same box B_1 . On the contrary, the central
310 position of FV_3 allows the corresponding jet to maintain longitudinal flow without deviation and thus
311 allows better internal ventilation of the whole pallet.

312 These strong short-circuits drive an important part of flow outside the pallet and directly affect
313 the ventilation of the downstream part of the pallet where high temperature levels are expected.

314 In the upstream part of the pallet related to boxes B_1 and B_2 , where forced convection
315 predominates, quasi-similar numerical and experimental velocity profiles are obtained regardless of the
316 intensity of the heat flux. The hybrid approach gives more accurate results than the direct CFD approach.
317 This concerns velocity profiles, peak positions and peak levels (see Fig. 4).

318 In the downstream part of the pallet, in Box B_3 , lower velocities were obtained due to the
319 deflection mechanism discussed above. More accurate results were also obtained for the hybrid approach
320 in comparison with the direct CFD approach for both heat fluxes. Whereas there was good agreement
321 between the hybrid approach and experimental results for the low heat flux ($Q = 0.05$ W), there were
322 some discrepancies for the high heat flux ($Q = 0.3$ W) which gave rise to reverse flow with low and
323 negative velocities mainly induced by secondary natural airflow circulation (Pham et al., 2021).
324 Obviously, both numerical approaches failed to predict local reverse flows associated with negative
325 velocities. This could be explained by both the complexity of a flow highly dominated by thermal
326 instability induced by dynamic interactions between vertical thermal plumes and the horizontal main
327 flow occurring in relatively stagnant areas, which can be accentuated at higher heat fluxes ($Q = 0.3$ W)
328 (Pham et al., 2021). However, the two-equation turbulence models (standard $k-\epsilon$ model) based on the
329 eddy viscosity tend to increase the numerical diffusion to ensure their numerical stability and thus are
330 unable to predict complex secondary flows.

331 Concerning overall differences between the experimental and numerical values, it is important
332 to note that the roughness of the primary packaging of the cheese, the imperfections in the arrangement,
333 and the presence of several resistance heating cables and thermocouples inside the boxes between the

334 cheeses influenced the experimental results. Also, the vent holes were not perfectly aligned between two
 335 successive boxes, which may have decreased the air passage area. These factors, which increase the
 336 pressure losses and limit the airflow, were not considered in the modelling, leading to an overestimation
 337 of the velocity in box B₃. Furthermore, the numerical error propagates in the model. The numerical error
 338 on L₁ will be reflected on L₂. As for the numerical velocity through L₃, besides its individual error, it
 339 will include the numerical error of L₁ and L₂.

340 3.1.2 Temperature distribution

341 The thermal validation of the model was performed using the product temperature profile along
 342 the line L_T (see Fig. 1). The profiles of the temperature difference with the incoming air ($\Delta T = T_p -$
 343 $T_{\text{air.in}}$) were investigated for two air upwind velocities, 0.31 m/s and 0.73 m/s, for three heat fluxes 0.05
 344 W, 0.15 W, and 0.3 W. Fig. 6 shows the experimental data, the hybrid approach and the direct CFD
 345 approach results.

346

347 The apparent differences that can be observed between the direct CFD and hybrid approach
 348 plots (Fig. 6) are related to their geometrical and volumetric heat generation representation. For the
 349 direct CFD approach, the cylindrical shape of the products was modelled and the heat is generated on
 350 each cheese position. The heat transfer between the air and cheese is achieved directly at the outer
 351 surface. Thus, the product temperature is highest in the centre of each product. Meanwhile, the hybrid
 352 approach modelled the box content as a porous medium with a parallelepiped shape associated with
 353 uniform properties such as the uniform heat generation per total volume of each porous zone. It tended
 354 to uniformise the temperature plots along the line L_T.

355 Table 3 presents the RMSE and the $\Delta T_{\text{max.exp}}$ for each configuration. In the case of lower inlet
 356 velocity 0.31 m/s, the corresponding RMSE values are 0.30°C, 0.37°C, and 0.95°C for 0.05 W, 0.15 W
 357 and 0.3 W, respectively. The RMSE values were relatively low in comparison with the maximum
 358 temperature difference between the product and the air: $\text{RMSE}/\Delta T_{\text{max.exp}}$ varies between 4% and 8%.

359

Table 3: Estimation of the RMSE and the maximum experimental temperature differential for the hybrid approach.

$u_{\text{air.in}}$ (m/s)	Q (W)	RMSE (°C)	$\Delta T_{\text{max.exp}}$ (°C)
0.31	0.05	0.30	3.71
	0.15	0.37	9.32
	0.3	0.95	16.57
0.73	0.05	0.41	2.25
	0.15	1.16	6.05
	0.3	2.25	11.52

360 For the highest air velocity, 0.73 m/s, unlike the direct CFD approach, the temperature
361 distribution obtained using the hybrid approach was underestimated compared to the experimental data
362 and $RMSE/\Delta T_{max.exp}$ was around 20%. This can be explained by the local thermal equilibrium hypothesis
363 (LTE) assumed by the porous medium model, which supposes an infinite convective heat transfer
364 coefficient between air and solid phases. Thus, the temperatures of these two phases are considered
365 equal in a representative elementary volume (REV) (Nield and Bejan, 2017). However, the experimental
366 results obtained by Pham et al. (2019) clearly indicate that for products generating heat, their
367 temperature becomes higher than that of the surrounding air. The difference increased with heat
368 generation and could reach about 2°C, which is comparable with the underestimation of the hybrid
369 approach in the worst case. This suggests that an improvement could be obtained using a two-
370 temperature porous medium approach instead of LTE. However, this implies estimating the local heat
371 transfer coefficient between the air and solid phases, which is a complex task because it depends on
372 local velocity magnitude, velocity orientation and turbulence (Alvarez and Flick, 1999).

373 As shown in Fig. 6, at a velocity of 0.73 m/s, temperature drops can be observed downstream
374 from the inlet of each box. To explain this phenomenon, Fig. 7 depicts the pathlines of the airflow on
375 three vertical planes, P_1 , P_2 and P_3 , passing by the centre of the front vents FV_1 , FV_2 and FV_3 ,
376 respectively. The temperature along the line L_T is measured on the plane P_2 (see Fig. 7b). This figure
377 shows a complex interaction between the flow in the air gap ($z > 120$ mm) and in the porous zone (air
378 + solid). Air flows faster in the air gap and is colder than in the porous zone. This is explained by the
379 fact that flow resistance and heat generation are located in the porous zone alone. Just after the front
380 face of a box, there is an entrainment effect exerted by the jets generated downstream from the upper
381 front vents (FV_1 , FV_2 and FV_3). A depression appears (suction effect): as can be seen on Fig. 7c, just
382 after the front face ($x < 5$ cm), the pressure is lower compared to that in the middle of the box. Warm
383 air from the porous zone flows upwards toward the jets and is replaced by cold air coming from the air
384 gap. This recirculation explains the temperature drops in Fig. 6. This effect (intensive mixing between
385 the air gap and the porous zone) is perhaps over-predicted by the hybrid approach model so that overall,
386 the temperature on line L_T is underestimated.

387 Fig. 8 presents the inflow rates through the different front vents compared to the total inflow
388 rate of B_1 . It can be seen that the sum of inflow rates through the front vents is not 100% in box B_1
389 because there is also a lateral inflow (as shown in Fig. 5b). The upper front vents have the greatest effect,
390 whereas the lower ones exert less effects because of obstacles behind them. This also explains the much
391 lower temperature in the air gap ($z > 120$ mm).

392 It appears that the exchange between the air gap zone and the porous zone is of major importance
393 for heat evacuation. Therefore, the airflow rate, related to the vertical velocity component, between the
394 two zones was calculated by Eq. (14) (upward flow compensates overall downflow in a box). It
395 decreases along the three boxes in the ventilation direction. For the case where $u_{air.in} = 0.73$ m/s and $Q =$
396 0.3 W, it is 1.38 L/s, 0.99 L/s and 0.55 L/s from the first to the last box.

$$\phi_{z.in} = \frac{1}{2} \int |u_z| dS_{interface} \quad (14)$$

397 It can be observed that the recirculation shown in plane P_2 has a limited spatial effect near the
398 principal vent FV_2 (Fig. 7b) and is not observed on the P_1 and P_3 planes. Therefore, only a limited area
399 of the first row of cheeses in the box is affected by the temperature drop, as can be seen in the temperature
400 contours shown in Fig. 9 (horizontal plane at $z = 75$ mm, in the porous zone). This also means that
401 despite this local temperature drop, the overall thermal behaviour indicates quasi-homogeneity of the
402 temperature row by row through the three boxes. This finding agrees with the results obtained by Pham
403 et al. (2021), which demonstrated that the temperature distribution in the same row of cheeses was
404 almost homogeneous.

405 According to the results presented in Fig. 6 and the temperature contours in Fig. 9, the
406 temperature distribution is related to the airflow rate, the product positions and the heat flow the products
407 generate. The higher the air velocity, the more heat is extracted from the products. According to Section
408 3.1.1 above, air heats up, and its velocity decreases in the main airflow direction, leading to better
409 cooling in the upstream than in the downstream box (Fig. 6). The heat flux generated by the cheeses also
410 significantly impacts the product temperature. The higher the heat flux, the higher the product
411 temperature. For example, at an air velocity of 0.31 m/s, the cheese in position C_6 (Fig. 1) is at 7.3°C
412 and 21.9°C for the two heat fluxes, 0.05 W and 0.3 W respectively, for inlet air at $T_{air.in} = 4^\circ\text{C}$. However,
413 because of free convection which enhances transfer, the effect is not linear. Indeed, when the heat flux
414 was six times higher, there was a three-fold rise in $T_p - T_{air.in}$. This aspect is of major importance, since
415 heat generation by cheeses is influenced by the temperature of the cheeses (Leclercq-Perlat et al., 2012).
416 Therefore, if the pallet temperature is not properly maintained at a target temperature, heat generation
417 may increase, thereby increasing the temperature of the cheeses, leading to a thermal runaway (Zhang
418 et al., 2018). A more detailed study is needed in order to establish a relationship between cheese heat
419 generation, temperature distribution, and mixed convection in a pallet in order to reduce losses and
420 ensure product quality which can be related to different factors such as cheese odour, colour and its crust
421 (underrind) thickness and consistency (Leclercq-Perlat et al., 2015).

422 3.1.3 Hybrid approach advantages and limitations

423 The results of this study showed the benefits of the hybrid approach, but also highlighted some
424 limitations that could be further studied. The major difference between hybrid and direct approach is
425 related to dynamic interactions between local air jets issuing vent holes and the physical objects
426 representing packed products. Small products randomly distributed behave as porous media while bigger
427 physical objects associated to higher velocities will affect in a specific manner the air jet development
428 leading to local obstructions, jet deviations and preferential airflow pathways within the ventilated
429 package.

430 To better extend the use of the hybrid approach to the products, future numerical and
431 experimental studies could investigate different extreme cases combining for example different specific
432 ventilated boxes (centrally and edge-positioned vents), different packaging pattern (layered packed
433 products with specific horizontal air paths and randomly packed products) and products of different size.
434 Comparisons between experimental and predicted values obtained with hybrid approach with different
435 velocities will help to assess and to validate the hybrid approach for other type of products while
436 underlying its limitation.

437 Finally, hybrid approach can be applied on a larger scale (entire cold room, truck) upon
438 validation and conduct more accurate multiscale simulation describing both airflow at the equipment
439 scale and detailed heat transfer in the pallets.

440 **4. Conclusion**

441 An original hybrid numerical approach was developed and applied to one pallet level of heat-
442 generating cheese under steady-state conditions. The results agreed acceptably with the direct CFD
443 approach results and experimental data regarding air velocity and product temperature. This method
444 reduced the computational time by a factor of 12 compared to the direct CFD approach. The hybrid
445 approach accurately characterises the preferential flow paths and temperature heterogeneity within the
446 pallet through the detailed modelling of the boxes (position and shape of the vent holes). It provides a
447 clear insight into the effect of mixed convection on temperature distribution.

448 The model will be improved by incorporating the local convective heat transfer coefficient and
449 assuming Local Thermal Non-Equilibrium. Further investigations using this approach will be conducted
450 to study the heating and cooling kinetics of heat-generating products within an entire pallet under
451 transient state conditions. Since the box vents are modelled, the method can be generalised for the study
452 of the adjacent pallets effect on the distribution of airflow and temperature within the pallets.

453 **Acknowledgements**

454 The authors acknowledge and thank the French Dairy Interbranch Organization (CNIEL) and
455 the French National Association of Research and Technology (ANRT) for the technical and financial
456 support that they have provided. The authors would like to thank the project coordinator Fanny
457 Tenenhaus-Aziza for her support.

458 **References**

- 459 Alvarez, G., Bournet, P.-E., Flick, D., 2003. Two-dimensional simulation of turbulent flow and transfer
460 through stacked spheres. *International Journal of Heat and Mass Transfer* 46, 2459–2469.
461 [https://doi.org/10.1016/S0017-9310\(02\)00546-X](https://doi.org/10.1016/S0017-9310(02)00546-X)
462 Alvarez, G., Flick, D., 1999. Analysis of heterogeneous cooling of agricultural products inside bins: Part
463 II: thermal study. *Journal of Food Engineering* 39, 239–245. [https://doi.org/10.1016/S0260-](https://doi.org/10.1016/S0260-8774(98)00166-6)
464 [8774\(98\)00166-6](https://doi.org/10.1016/S0260-8774(98)00166-6)

465 Ambaw, A., Mukama, M., Opara, U.L., 2017. Analysis of the effects of package design on the rate and
466 uniformity of cooling of stacked pomegranates: Numerical and experimental studies. *Computers
467 and Electronics in Agriculture* 136, 13–24. <https://doi.org/10.1016/j.compag.2017.02.015>

468 Bejan, A., 2013. *Convection Heat Transfer*. John Wiley & Sons.

469 Berry, T.M., Defraeye, T., Wu, W., Sibiyi, M.G., North, J., Cronje, P.J.R., 2021. Cooling of ambient-
470 loaded citrus in refrigerated containers: What impacts do packaging and loading temperature
471 have? *Biosystems Engineering* 201, 11–22.
472 <https://doi.org/10.1016/j.biosystemseng.2020.11.002>

473 Chourasia, M.K., Goswami, T.K., 2007. CFD simulation of effects of operating parameters and product
474 on heat transfer and moisture loss in the stack of bagged potatoes. *Journal of Food Engineering*
475 80, 947–960. <https://doi.org/10.1016/j.jfoodeng.2006.07.015>

476 Defraeye, T., Lukasse, L., Shrivastava, C., Verreydt, C., Schemminger, J., Cronjé, P., Berry, T., 2022.
477 Is there a systematic hidden “hot spot” in refrigerated containers filled with fresh food in
478 ventilated packaging? *Trends in Food Science & Technology* 129, 388–396.
479 <https://doi.org/10.1016/j.tifs.2022.09.005>

480 Delahaye, A., Gahartian, J., Jouquin, C., Oignet, J., Ndoye, F.T., 2019. Dispositif de calorimétrie pour
481 la mesure de flux de chaleur dégagés au cours de l’entreposage de fromages.

482 Delele, M.A., Ngcobo, M.E.K., Opara, U.L., Meyer, C.J., 2013. Investigating the Effects of Table Grape
483 Package Components and Stacking on Airflow, Heat and Mass Transfer Using 3-D CFD
484 Modelling. *Food Bioprocess Technol* 6, 2571–2585. <https://doi.org/10.1007/s11947-012-0895-5>

485

486 Duret, S., Hoang, H.-M., Flick, D., Laguerre, O., 2014. Experimental characterization of airflow, heat
487 and mass transfer in a cold room filled with food products. *International Journal of Refrigeration*
488 46, 17–25. <https://doi.org/10.1016/j.ijrefrig.2014.07.008>

489 Einfeld, B., Schnitzlein, K., 2001. The influence of confining walls on the pressure drop in packed beds.
490 *Chemical Engineering Science* 56, 4321–4329. [https://doi.org/10.1016/S0009-2509\(00\)00533-9](https://doi.org/10.1016/S0009-2509(00)00533-9)

491

492 Ferrua, M.J., Singh, R.P., 2008. A nonintrusive flow measurement technique to validate the simulated
493 laminar fluid flow in a packed container with vented walls. *International Journal of
494 Refrigeration* 31, 242–255. <https://doi.org/10.1016/j.ijrefrig.2007.05.013>

495 Gaucel, S., Guillemin, H., Corrieu, G., 2012. A generalised model for cheese mass loss determination
496 during ripening. *Journal of Food Engineering* 110, 109–116.
497 <https://doi.org/10.1016/j.jfoodeng.2011.12.002>

498 Han, J.-W., Zhao, C.-J., Qian, J.-P., Luis, R.-G., Xiang, Z., 2018. Numerical modeling of forced-air
499 cooling of palletized apple: Integral evaluation of cooling efficiency. *International Journal of
500 Refrigeration* 11.

501 Han, J.-W., Zhao, C.-J., Yang, X.-T., Qian, J.-P., Fan, B.-L., 2015. Computational modeling of airflow
502 and heat transfer in a vented box during cooling: Optimal package design. *Applied Thermal
503 Engineering* 91, 883–893. <https://doi.org/10.1016/j.applthermaleng.2015.08.060>

504 Hélias, A., Mirade, P.-S., Corrieu, G., 2007. Modeling of Camembert-Type Cheese Mass Loss in a
505 Ripening Chamber: Main Biological and Physical Phenomena. *Journal of Dairy Science* 90,
506 5324–5333. <https://doi.org/10.3168/jds.2007-0272>

507 Hélias, A., Trelea, I.C., Corrieu, G., 2008. Assessment of respiratory activity during surface-mould
508 cheese ripening. *Journal of Food Engineering* 85, 632–638.
509 <https://doi.org/10.1016/j.jfoodeng.2007.09.001>

510 Ho, S.H., Rahman, M.M., Sunol, A.K., 2010. Analysis of thermal response of a food self-heating system.
511 *Applied Thermal Engineering* 30, 2109–2115.
512 <https://doi.org/10.1016/j.applthermaleng.2010.05.020>

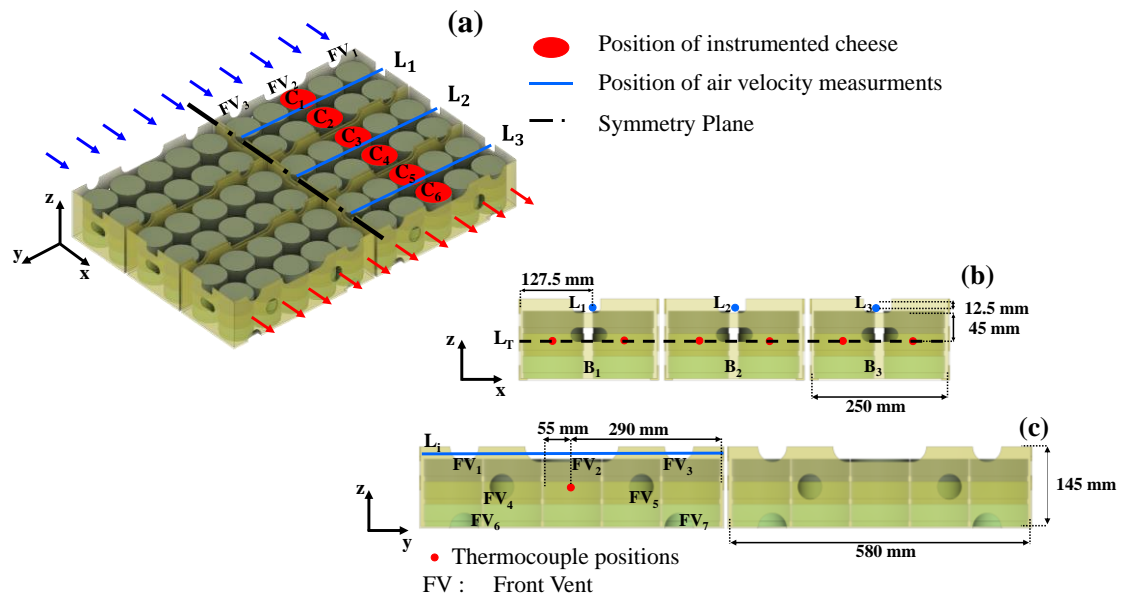
513 Hoang, H.-M., Duret, S., Flick, D., Laguerre, O., 2015. Preliminary study of airflow and heat transfer
514 in a cold room filled with apple pallets: Comparison between two modelling approaches and
515 experimental results. *Applied Thermal Engineering* 76, 367–381.
516 <https://doi.org/10.1016/j.applthermaleng.2014.11.012>

517 Iezzi, R., Francolino, S., Mucchetti, G., 2011. Natural convective cooling of cheese: Predictive model
518 and validation of heat exchange simulation. *Journal of Food Engineering* 106, 88–94.
519 <https://doi.org/10.1016/j.jfoodeng.2011.04.016>

520 Leclercq-Perlat, M.-N., Sicard, M., Perrot, N., Trelea, I.C., Picque, D., Corrieu, G., 2015. Temperature
521 and relative humidity influence the ripening descriptors of Camembert-type cheeses throughout
522 ripening. *Journal of Dairy Science* 98, 1325–1335. <https://doi.org/10.3168/jds.2014-8916>
523 Leclercq-Perlat, M.-N., Sicard, M., Trelea, I.C., Picque, D., Corrieu, G., 2012. Temperature and relative
524 humidity influence the microbial and physicochemical characteristics of Camembert-type
525 cheese ripening. *Journal of Dairy Science* 95, 4666–4682. <https://doi.org/10.3168/jds.2012-5368>
526
527 Moureh, J., Tapsoba, M., Flick, D., 2009a. Airflow in a slot-ventilated enclosure partially filled with
528 porous boxes: Part I – Measurements and simulations in the clear region. *Computers & Fluids*
529 38, 194–205. <https://doi.org/10.1016/j.compfluid.2008.02.006>
530 Moureh, J., Tapsoba, S., Derens, E., Flick, D., 2009b. Air velocity characteristics within vented pallets
531 loaded in a refrigerated vehicle with and without air ducts. *International Journal of Refrigeration*
532 32, 220–234. <https://doi.org/10.1016/j.ijrefrig.2008.06.006>
533 Nield, D.A., Bejan, A., 2017. *Convection in Porous Media*. Springer International Publishing, Cham.
534 <https://doi.org/10.1007/978-3-319-49562-0>
535 O’Sullivan, J.L., Ferrua, M.J., Love, R., Verboven, P., Nicolai, B., East, A., 2017. Forced-air cooling of
536 polylined horticultural produce: Optimal cooling conditions and package design. *Postharvest*
537 *Biology and Technology* 126, 67–75. <https://doi.org/10.1016/j.postharvbio.2016.11.019>
538 Pham, A.T., 2021. Caractérisation aéraulique et thermique au sein d’un empilement de produits
539 dégageant de la chaleur: application au cas des palettes de fromage. *Agriculture, alimentation,*
540 *biologie, environnement et santé*.
541 Pham, A.T., Moureh, J., Belaidi, M., Flick, D., 2021. CFD modelling of a pallet of heat-generating
542 product applied to a cheese product. *International Journal of Refrigeration* 128, 163–176.
543 <https://doi.org/10.1016/j.ijrefrig.2021.03.011>
544 Pham, A.T., Moureh, J., Flick, D., 2019. Experimental characterization of heat transfer within a pallet
545 of product generating heat. *Journal of Food Engineering* 247, 115–125.
546 <https://doi.org/10.1016/j.jfoodeng.2018.12.003>
547 Praeger, U., Jedermann, R., Sellwig, M., Neuwald, D.A., Hartgenbusch, N., Borysov, M., Truppel, I.,
548 Scaar, H., Geyer, M., 2020. Airflow distribution in an apple storage room. *Journal of Food*
549 *Engineering* 269, 109746. <https://doi.org/10.1016/j.jfoodeng.2019.109746>
550 Redding, G.P., Yang, A., Shim, Y.M., Olatunji, J., East, A., 2016. A review of the use and design of
551 produce simulators for horticultural forced-air cooling studies. *Journal of Food Engineering*
552 190, 80–93. <https://doi.org/10.1016/j.jfoodeng.2016.06.014>
553 Verboven, P., Flick, D., Nicolai, B.M., Alvarez, G., 2006. Modelling transport phenomena in
554 refrigerated food bulks, packages and stacks: basics and advances. *International Journal of*
555 *Refrigeration, Issue with Special Emphasis on Data and Models on Food Refrigeration* 29, 985–
556 997. <https://doi.org/10.1016/j.ijrefrig.2005.12.010>
557 Wang, D., Lai, Y., Jia, B., Chen, R., Hui, X., 2020. The optimal design and energy consumption analysis
558 of forced air pre-cooling packaging system. *Applied Thermal Engineering* 165, 114592.
559 <https://doi.org/10.1016/j.applthermaleng.2019.114592>
560 Wu, W., Beretta, C., Cronje, P., Hellweg, S., Defraeye, T., 2019. Environmental trade-offs in fresh-fruit
561 cold chains by combining virtual cold chains with life cycle assessment. *Applied Energy* 254,
562 113586. <https://doi.org/10.1016/j.apenergy.2019.113586>
563 Zhang, K., Pu, Y.-Y., Sun, D.-W., 2018. Recent advances in quality preservation of postharvest
564 mushrooms (*Agaricus bisporus*): A review. *Trends in Food Science & Technology* 78, 72–82.
565 <https://doi.org/10.1016/j.tifs.2018.05.012>
566 Zhao, C.-J., Han, J.-W., Yang, X.-T., Qian, J.-P., Fan, B.-L., 2016. A review of computational fluid
567 dynamics for forced-air cooling process. *Applied Energy* 168, 314–331.
568 <https://doi.org/10.1016/j.apenergy.2016.01.101>
569 Zou, Q., Opara, L.U., McKibbin, R., 2006a. A CFD modeling system for airflow and heat transfer in
570 ventilated packaging for fresh foods: I. Initial analysis and development of mathematical
571 models. *Journal of Food Engineering* 77, 1037–1047.
572 <https://doi.org/10.1016/j.jfoodeng.2005.08.042>
573 Zou, Q., Opara, L.U., McKibbin, R., 2006b. A CFD modeling system for airflow and heat transfer in
574 ventilated packaging for fresh foods: II. Computational solution, software development, and

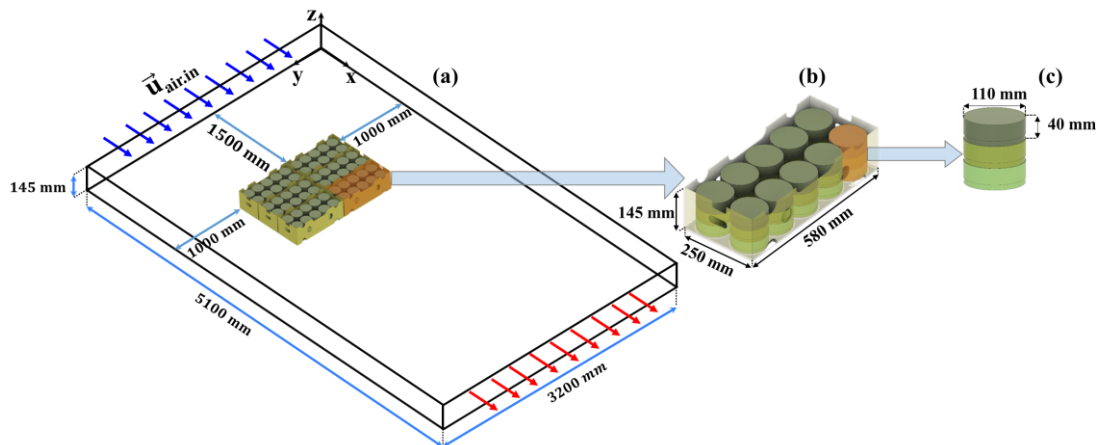
575 model testing. Journal of Food Engineering 77, 1048–1058.
576 <https://doi.org/10.1016/j.jfoodeng.2005.08.043>
577
578

579



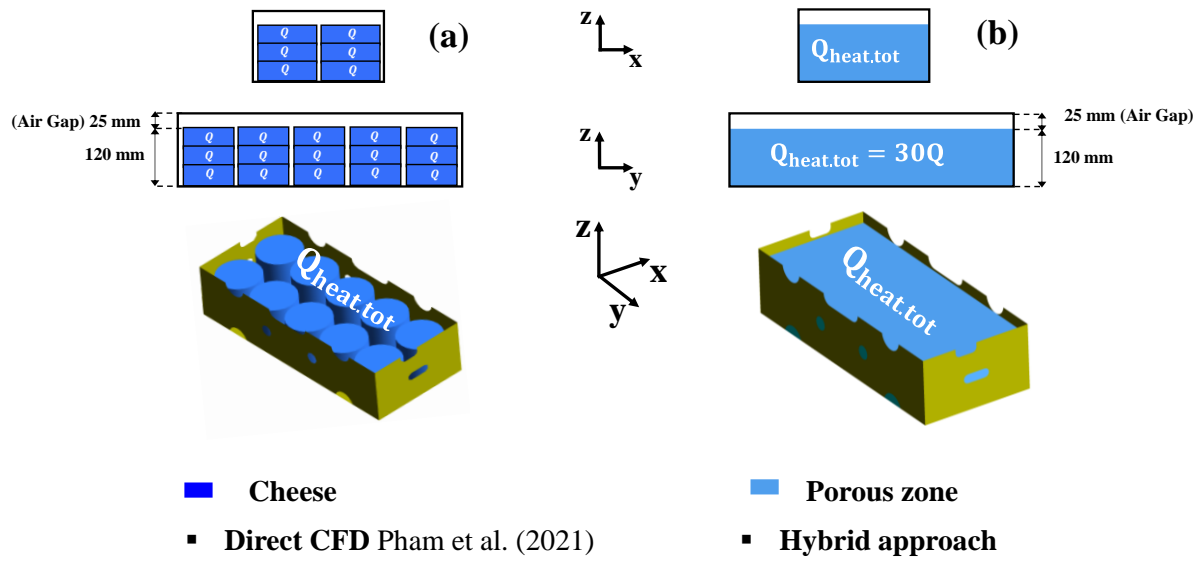
580

581 Fig. 1. Illustration of the instrumented level of the pallet and its dimensions: (a) 3D view; (b) front view; and (c) lateral view.



582

583 Fig. 2. Illustration of (a) the computational domain of the model; (b) the dimensions of the cardboard boxes; and (c) the
584 dimensions of the cheese cylinders.



585

586

Fig. 3. Comparison between (a) direct CFD (Pham et al., 2021), and (b) hybrid approach geometry representation.

587

588

589

590

591

592

593

594

595

596

597

598

599

600

601

602

603

604

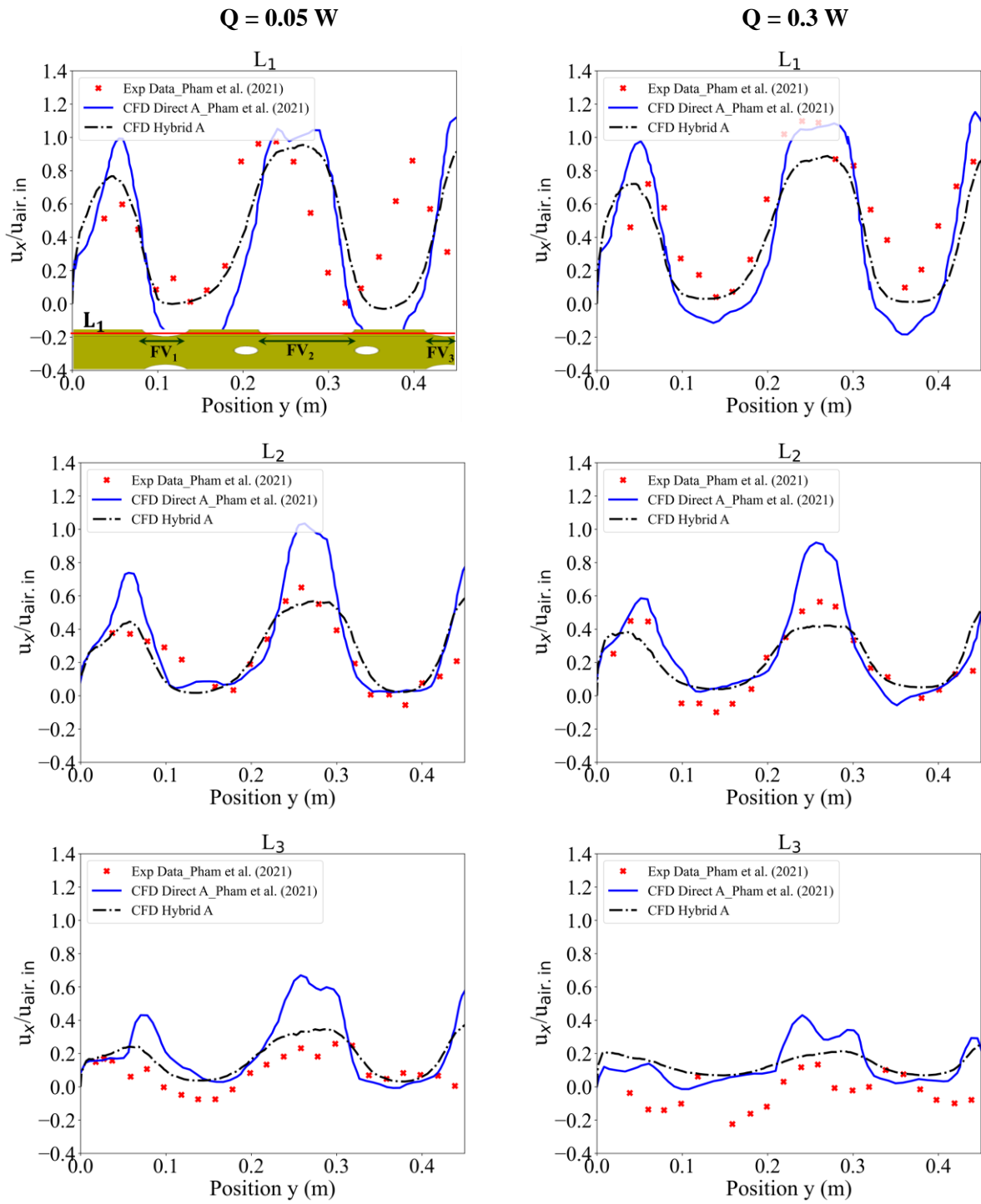
605

606

607

608

609



610 Fig. 4. Comparison of the air gap transversal velocity through the lines L_1 , L_2 and L_3 for inlet velocity 0.31 m/s and two heat
 611 generation fluxes, 0.05 W and 0.3 W, with both experimental data and direct CFD approach results of Pham et al. (2021).

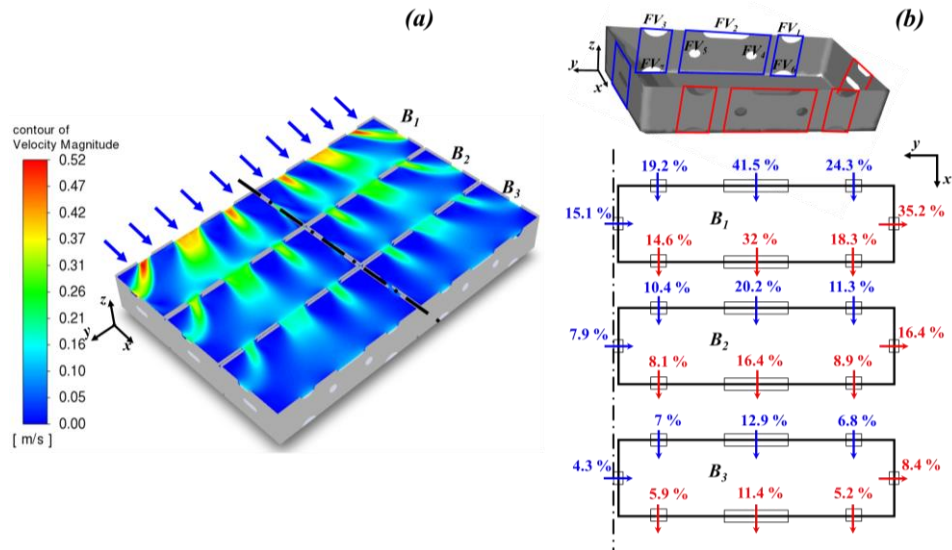


Fig. 5. Airflow distribution through the boxes for $u_{air.in} = 0.31$ m/s and $Q = 0W$; (a) air velocity magnitude at $z = 132.5$ mm; (b) inflow and outflow rates compared to a total inflow of box B_1 .

612
613
614

615

616

617

618

619

620

621

622

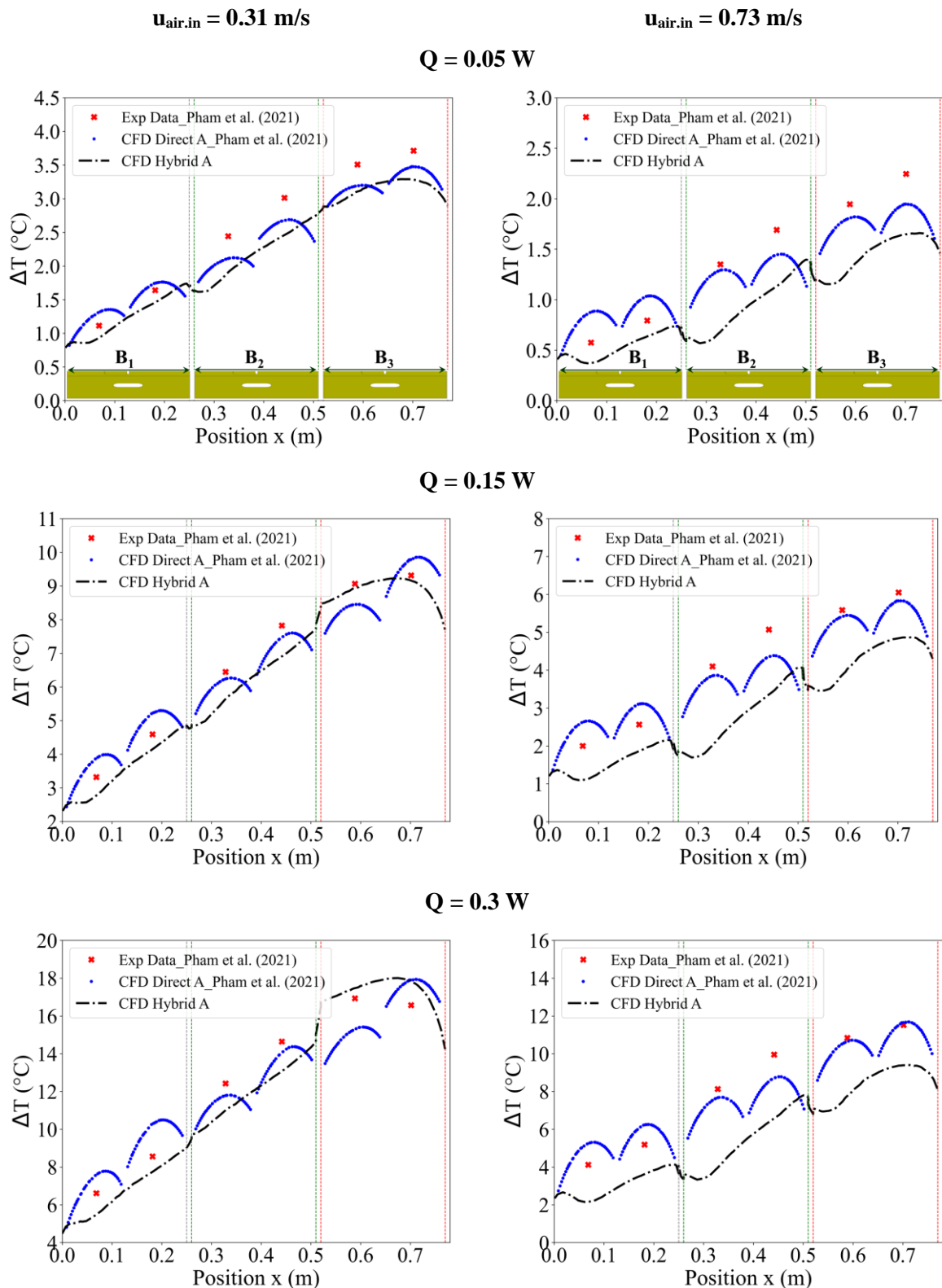
623

624

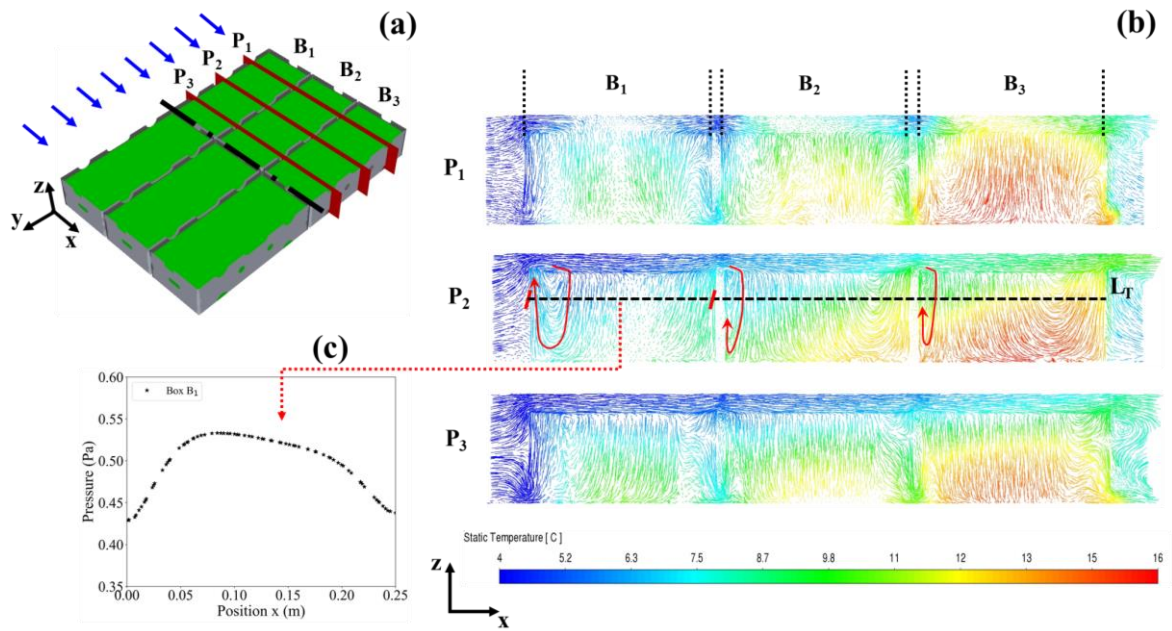
625

626

627



628 Fig. 6. Comparison of the temperature difference distribution ($\Delta T = T_p - T_{\text{air.in}}$) obtained with the hybrid approach through the
 629 line L_T for air inlet velocities 0.31 m/s and 0.73 m/s and three heat fluxes, 0.05 W, 0.15 W and 0.3 W, with both experimental
 630 data and direct CFD results of Pham et al. (2021). Note: Experimental data of Pham et al. (2021) (red cross); direct CFD
 631 results of Pham et al. (2021) (blue points) and hybrid approach results (black dashed line). The dashed grey, green and red
 632 vertical lines used delimit boxes B_1 , B_2 and B_3 , respectively.



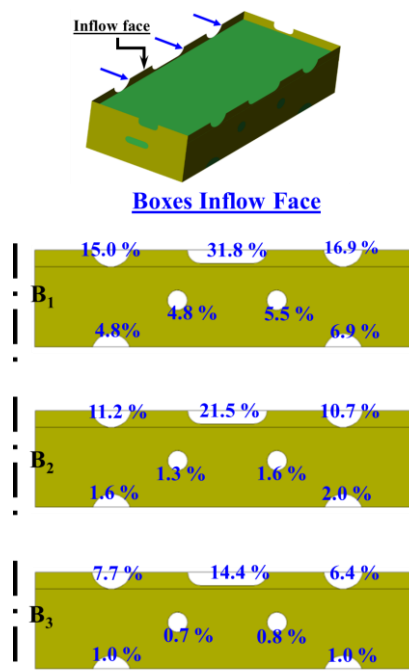
634

635

636

Fig. 7. (a) Diagram showing the positions of the planes; (b) Airflow pathlines coloured by the temperature through three planes P₁, P₂ and P₃ for $u_{air,in} = 0.73$ m/s and $Q=0.3$ W; (c) pressure evolution through the line L_r in the box B₁.

637

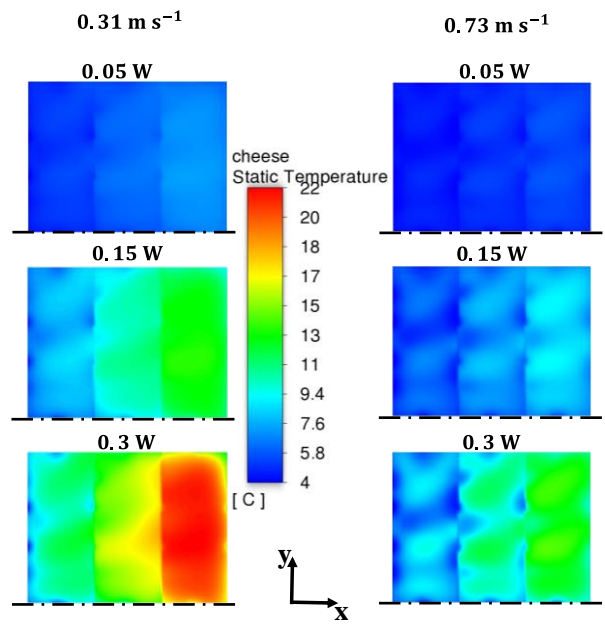


638

639

640

Fig. 8. Airflow rates in the different front vents of the boxes compared to the total inflow rate of box B₁ $u_{air,in} = 0.73$ m/s $Q = 0.3$ W.



641

642
643

Fig. 9. Temperature distribution for two airflow velocities, 0.31 m/s and 0.73 m/s, and three heat-generated fluxes, 0.05 W, 0.15 W and 0.3 W (horizontal plane at $z = 75 \text{ mm}$).